Triggering phase-coherent spin packets by pulsed electrical spin injection across an Fe/GaAs Schottky barrier

L. R. Schreiber,[1,2] C. Schwark,[1] G. Güntherodt,[1] M. Lepsa,[3] C. Adelmann,[4,5] C. J. Palmstrøm,[4,6] X. Lou,[7] P. A. Crowell,[7] and B. Beschoten[1,*]

[1]*2nd Institute of Physics and JARA-FIT, RWTH Aachen University, 52074 Aachen, Germany*
[2]*JARA-FIT Institute for Quantum Information, Forschungszentrum Jülich GmbH and RWTH Aachen University, 52074 Aachen, Germany*
[3]*Peter Grünberg Institute (PGI-10), Forschungszentrum Jülich GmbH, 52425 Jülich, Germany*
[4]*Department of Chemical Engineering and Material Science, University of Minnesota, Minneapolis, Minnesota 55455, USA*
[5]*IMEC, 3001 Leuven, Belgium*
[6]*Departments of Electrical and Computer Engineering and Materials, University of California, Santa Barbara, California 93106, USA*
[7]*School of Physics and Astronomy, University of Minnesota, Minneapolis, Minnesota 55455, USA*

(Received 2 September 2021; revised 8 November 2021; accepted 8 November 2021; published 19 November 2021)

The precise control of spins in semiconductor spintronic devices requires electrical means to generate spin packets with a well-defined initial phase. We demonstrate a pulsed electrical scheme that triggers the spin ensemble phase in a similar way as circularly polarized optical pulses generate phase coherent spin packets. Here, we use fast current pulses to initialize phase coherent spin packets, which are injected across an Fe/GaAs Schottky barrier into *n*-GaAs. By means of time-resolved Faraday rotation, we demonstrate phase coherence by the observation of multiple Larmor precession cycles for current pulse widths down to 500 ps at 17 K. We show that the current pulses are broadened by the charging and discharging time of the Schottky barrier. At high frequencies, the observable spin coherence is limited only by the finite bandwidth of the current pulses, which is of the order of 2 GHz. These results therefore demonstrate that all-electrical injection and phase control of electron spin packets at microwave frequencies is possible in metallic-ferromagnet–semiconductor heterostructures.

DOI: 10.1103/PhysRevB.104.195202

I. INTRODUCTION

The preparation and phase-controlled manipulation of coherent single spin states or spin ensembles is fundamental for spintronic devices [1,2]. Devices based on electron spin ensembles require for spin coherence an initial triggering of the phase of all the individual spins, which results in a macroscopic phase of the ensemble. Such a phase triggering can easily be obtained by circularly polarized ultrafast laser pulses, which are typically shorter than one ps [3,4]. By impulsive laser excitation, all spins of the ensemble are oriented in the same direction, i.e., they are created with the same initial phase. Spin precession of the ensemble can be monitored by time-resolved magneto-optical probes as the spin precession time is usually orders of magnitude longer than the laser pulse width. Along with other techniques, these time-resolved all-optical methods have been used to detect spin dephasing times [3,5–7], strain-induced spin precession [8,9], and phase-sensitive spin manipulation in lateral devices [8,10,11].

Spin precession can also be observed in dc transport experiments [12–17]. In spin injection devices, for example, electron spins are injected from a ferromagnetic source into a semiconductor [18–29]. Their initial spin orientation near the ferromagnet-semiconductor interface is defined by the magnetization direction of the ferromagnet. Individual spins start to precess in a transverse magnetic field. This results in a rapid depolarization of the steady-state spin polarization (the Hanle effect) because spins are injected continuously in the time domain. The precessional phase is preserved partially when there is a well-defined transit time between the source and the detector [12,15]. This has been achieved in Si by spin-polarized hot electron injection and detection techniques operated in a drift-dominated regime, which allowed for multiple spin precessions [15,16], while only very few precessions could be seen in GaAs-based devices [12,13]. On the other hand, pulsed electrical spin injection has been reported [26,27], but no spin precession was observed. Despite recent progress in realizing all-electrical spintronic devices, electrical phase triggering is missing.

Here, we use fast current pulses to trigger the ensemble phase of electrically generated spin packets during spin injection from a ferromagnetic source into a III-V semiconductor. Coherent precession of the spin packets is probed by time-resolved Faraday rotation. Our device consists of a highly doped Schottky tunnel barrier formed between an epitaxial iron (Fe) and a (100)-oriented *n*-GaAs layer. We chose this device design for three reasons: (i) the Schottky barrier profile guarantees large spin injection efficiencies [21,24,30,31], (ii) the *n*-GaAs layer is Si doped with carrier densities near the metal-insulator transition ($n = 2$–4×10^{16} cm^{-3}) which

*bernd.beschoten@physik.rwth-aachen.de

provides long spin dephasing times T_2^* for detection [3,32,33], and (iii) the Fe injector has a twofold magnetic in-plane anisotropy [34], which allows for a noncollinear alignment between the external magnetic field direction and the magnetization direction of the Fe layer and thus the spin direction of the injected spin packets. This noncollinear alignment is needed to induce Larmor precession of the spin ensemble. We observe spin precession of the electrically injected spin packets for current pulse widths down to 500 ps. The net magnetization of the spin packet diminishes with increasing magnetic field. We link this decrease to the high-frequency properties of the Schottky barrier. Its charging and discharging leads to a broadening of the current pulses and hence temporal broadening of the spin packet, as well as phase smearing during spin precession. We introduce a model for ultrafast electrical spin injection and extract a Schottky barrier time constant from our Faraday rotation data of 8 ± 2 ns, which is confirmed by independent high-frequency electrical characterization of our spin device.

II. EXPERIMENT

Our measurement setup and sample geometry are depicted in Fig. 1(a). The sample consists of an Al-capped, 3.5-nm-thick, epitaxially grown Fe(001) layer on n-doped Si:GaAs(001). The doping concentration of the 15-nm-thick n^+-GaAs layer starting at the Schottky contact is 5×10^{18} cm^{-3}, followed by a 15 nm n^+/n transition layer with a doping gradient, a 5-μm-thick bulk layer with doping concentration 2×10^{16} cm^{-3}, and a highly doped ($\sim 1 \times 10^{18}$ cm^{-3}) GaAs substrate [layer stack details in Fig. 3(c)]. The sample mesa with 650 μm radius is etched down to the substrate. The T_2^* of the substrate is smaller than 1 ns. The magnetic easy axis of the Fe layer is oriented along the GaAs [011] ($\pm x$ direction). A comparison of electrical and all-optical Hanle measurements indicates a spin injection efficiency into the bulk n-GaAs layer of $\sim$7% for a wide bias range. The differential resistance of the layer stack and the magnetic characterization of the Fe layer is shown in the Appendix.

Samples are mounted in a magneto-optical cryostat kept at 17 K with a magnetic field B_z oriented along the $\pm z$ direction. For time-resolved electrical spin injection, a voltage pulse train (amplitude 1.8 V) from a pulse generator (65 ps rise and fall time) is applied via a bias-tee to the sample, which is placed on a coplanar waveguide within a magneto-optical cryostat. Linearly polarized laser pulses at normal incidence to the sample plane and phase locked to the electrical pulses monitor the $\pm y$ component of spins injected in the GaAs by detecting the Faraday rotation angle θ_F. The linearly polarized laser pulses ($P = 200$ μW with a focus diameter $\approx$50 μm on the sample) are generated by a picosecond Ti-sapphire laser with a stabilized repetition frequency of 80 MHz. They are phase locked to the voltage pulses and can be delayed by a time Δt up to 125 ns with a variable phase shifter with ps resolution. The laser energy 1.508 eV is tuned to just below the band gap of the GaAs. The repetition interval of the pump and probe pulses can be altered from 12.5 to 125 ns by an optical pulse selector and the full width at half maximum Δw of the voltage pulses can be varied from 100 ps to 10 ns. Both pump and probe pulses are intensity modulated by 50 kHz and 820 Hz, respectively, in order to extract the pump induced θ_F signal by a dual lock-in technique.

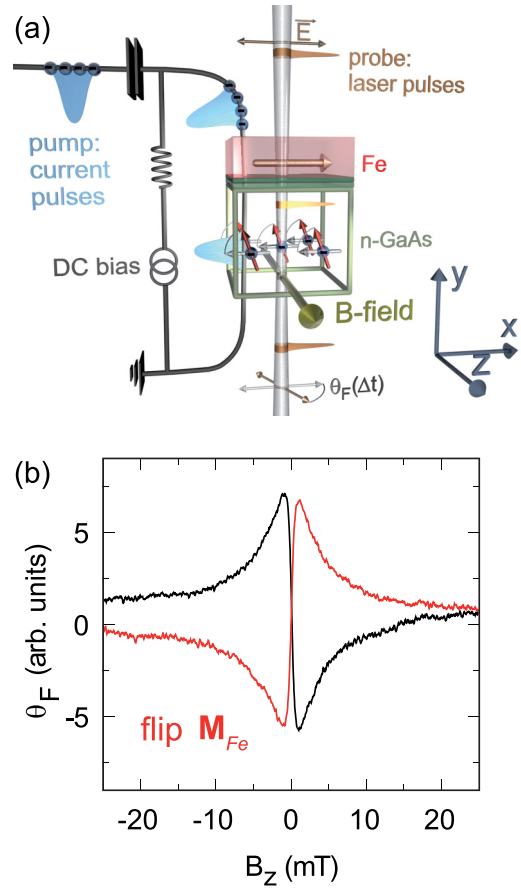

FIG. 1. Electrical pump and optical probe setup and test by continuous electrical injection. (a) Schematic of the electrical pump and optical probe experiment of spins injected from Fe into n-GaAs. (b) Faraday rotation θ_F (Hanle depolarization) of the dc current along the y direction as a function of the external transverse magnetic field B_z at constant bias before (black line) and after (red line) flipping the Fe magnetization $\mathbf{M}_{Fe}$.

III. RESULTS

A. Static spin injection

We first use static measurements of the Faraday rotation to demonstrate electrical spin injection in our devices [Fig. 1(b)]. The sample is reverse biased, i.e., positive voltage probe on GaAs, and spins are probed near the fundamental band gap of GaAs. At $B_z = 0$ T, spins are injected parallel to the easy-axis direction of the Fe layer, yielding $\theta_F = 0$. At small magnetic fields B_z, spins start to precess towards the y direction, yielding $\theta_F \neq 0$. θ_F is a direct measure of the resulting net spin component S_y. Changing the sign of B_z inverts the direction of the spin precession, which results in a sign reversal of θ_F. As expected [12], the direction of spin precession also inverts when the magnetization direction of the Fe layer is reversed [see red curve in Fig. 1(b)]. θ_F approaches zero at large fields since the continuously injected

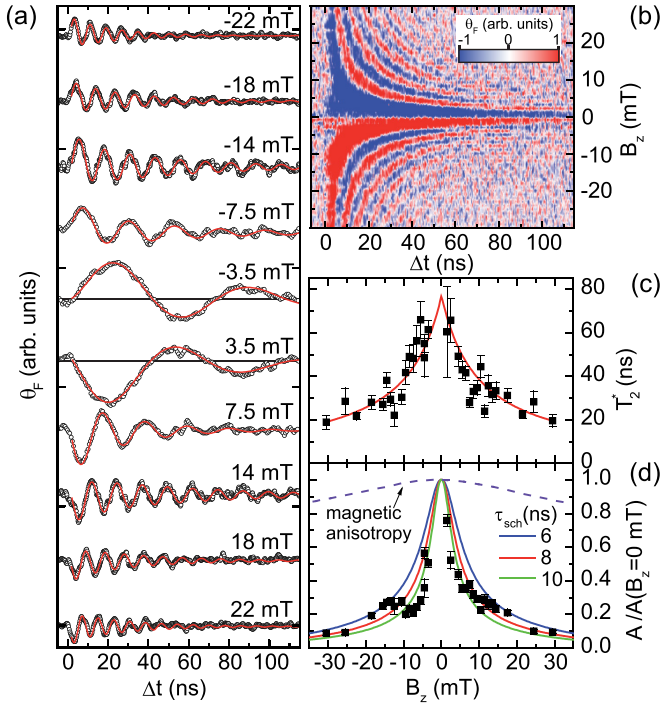

FIG. 2. Pulsed electrical spin injection. (a) Time evolution of the Faraday rotation θ_F vs pump-probe delay Δt for various magnetic fields B_z with vertical offsets for clarity. Red lines are fits to the data for $\Delta t > \Delta w = 2$ ns. (b) False color plot of θ_F vs Δt and B_z. (c) Fitted spin dephasing time $T_2^*(B_z)$ and (d) normalized oscillation amplitudes A vs B_z field. The error bars include the least-squares fit errors only. The red solid line in (c) is a least-squares fit to the data and solid lines in (d) are simulations for different effective charge and discharge times $\tau_{\rm sch}$ of the Schottky barrier. The dashed line is the expected decrease of A due to the magnetic anisotropy of the Fe injector layer.

spins dephase due to Larmor precession causing strong Hanle depolarization.

B. Time-resolved spin injection

For time-resolved spin injection experiments, we now apply voltage pulses with a full width at half maximum of $\Delta w = 2$ ns and a repetition time of $T_{\rm rep} = 125$ ns with $T_{\rm rep} > T_2^*$. The corresponding time-resolved Faraday rotation data are shown in Figs. 2(a) and 2(b) at various magnetic fields. Most strikingly, we clearly observe Larmor precessions of the injected spin packets demonstrating that the voltage pulses trigger the macrophase of the spin packets. It is apparent that the amplitude of θ_F is diminished with increasing $|B_z|$. We note that the oscillations in θ_F are not symmetric about the zero baseline [see black lines in Fig. 2(a) as guides to the eye]. For quantitative analysis, we use

$$\begin{aligned}\theta_F(\Delta t, B_z) &\propto M_y(\Delta t, B_z)\\ &= A(B_z)\exp\left[-\frac{\Delta t}{T_2^*(B_z)}\right]\sin(\omega_L \Delta t + \phi)\\ &\quad + A_{bg}(B_z)\exp\left(-\frac{\Delta t}{\tau_{bg}}\right),\end{aligned} \tag{1}$$

with $\omega_L = g\mu_B B/\hbar$, where g, μ_B, and $\hbar$ denote the effective electron g factor, the Bohr magneton, and the reduced Planck constant, and ϕ being a phase factor. The second term accounts for the nonoscillatory time-dependent background with a lifetime τ_{bg} and an amplitude A_{bg} (the magnetic field dependence of A_{bg} is shown in the Supplemental Material [35]). The least-squares fits to the experimental data are shown in Fig. 2(a) as red curves. We determine a field-independent $\tau_{bg} = 8 \pm 2$ ns and deduce $|g| = 0.42 \pm 0.02$ from ω_L as expected given that the spin precession is detected in the bulk n-GaAs layer [3]. The extracted spin dephasing times $T_2^*(B_z)$ and amplitudes $A(B_z)$ are plotted in Figs. 2(c) and 2(d), respectively. The longest $T_2^*(B_z)$ values, which exceed 65 ns, are obtained at small magnetic fields. The observed $1/B$ dependence of $T_2^*(B_z)$ [see red line in Fig. 2(c)], which indicates inhomogeneous dephasing of the spin packet, is consistent with the results obtained from all-optical time-resolved experiments on bulk samples with similar doping concentration [3]. On the other hand, the strong decrease of $A(B_z)$ with magnetic field [Fig. 2(d)] has not previously been observed in all-optical experiments. Note that spin precession is barely visible for magnetic fields above 30 mT.

The $A(B_z)$ dependence might be caused by the B_z field acting on the direction of the magnetization $\mathbf{M}_{Fe}$ of the Fe injector. Increasing B_z rotates $\mathbf{M}_{Fe}$ away from the easy axis (x direction) towards the hard axis (z direction) of the Fe layer. This rotation diminishes the x component of the magnetization vector of the injected spin packet, which would result in a decrease of $A(B_z)$. We calculated this dependence [see dashed line in Fig. 2(d)] for a macrospin $\mathbf{M}_{Fe}$ using in-plane magnetometry data from the Fe layer (see Fig. 6). The resulting decrease is, however, too small to explain our $A(B_z)$ dependence.

To summarize, there are two striking observations in our time-resolved electrical spin injection experiments: (i) the strong decrease of the Faraday rotation amplitude $A(B_z)$ and (ii) the nonoscillatory background in $\theta_F(\Delta t)$ with a field-independent time constant $\tau_{bg} = 8 \pm 2$ ns. As both have not been observed in time-resolved all-optical experiments, it is suggestive to link these properties to the dynamics of the electrical spin injection process.

In our time-resolved experiment, electron spin packets are injected across a Schottky barrier by short voltage pulses. The depletion layer at the barrier acts like a capacitance. When a voltage pulse is transmitted through the barrier, the capacitance will be charged and subsequently discharged. For studying the effect of the charging and discharging on the spin injection process, we performed high-frequency (HF) electrical characterization of our devices.

C. High-frequency sample characteristic

The HF bandwidth of the sample is deduced from the reflected electrical power S_{11} by vector network analysis, as shown in Fig. 3(a). More than half of the electrical power ($S_{11} > 3$ dB) is reflected from the device for frequencies above ~1.5 GHz. This bandwidth is independent of the operating point over a wide dc-bias range from −2.0 V (reverse biased Schottky contact) to 1.0 V and allows the sample to absorb voltage pulses of width $\Delta w \gtrsim 500$ ps.

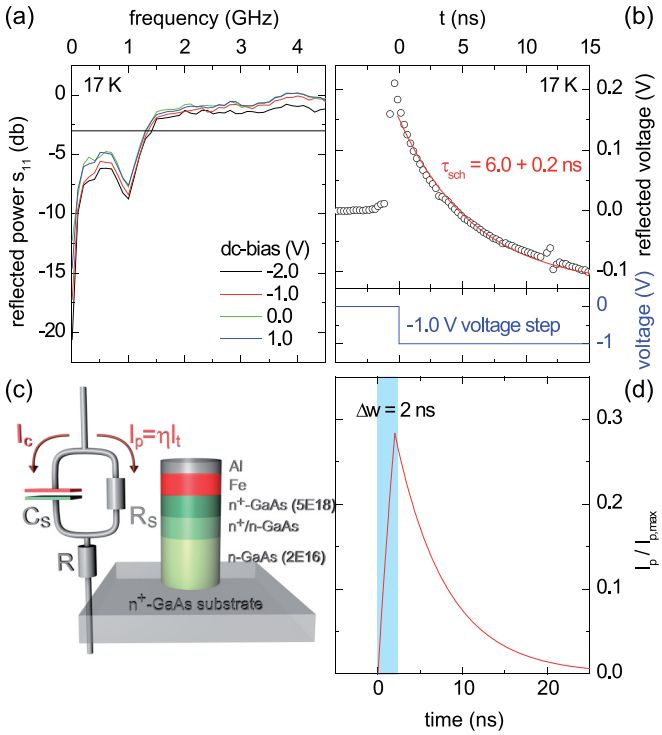

FIG. 3. Electrical high-frequency characterization. (a) Reflected power (S_{11}) for various dc-bias operating points obtained from vector network analysis. (b) Voltage reflected from the sample after applying a voltage step function (−1.0 V) with least-squares exponential fit (red solid line). (c) Sample structure and simple equivalent network of the sample. (d) Simulation (red line) of the evolution of the spin-polarized tunnel current through the Schottky barrier triggered by a 2-ns-long current pulse (light blue).

Furthermore, the time evolution of the voltage drop at the Schottky barrier, i.e., its charging and discharging, can directly be determined by time-domain reflectometry (TDR). To analyze the charging dynamics of the Schottky capacitance, we apply a voltage step to the sample with an amplitude of −1 V and a rise time of 100 ps. The time evolution of the reflected voltage step is shown in Fig. 3(b). Note that there is a significant temporal broadening of the voltage step. We obtain a similar time constant for the discharging behavior (not shown). Any impedance mismatch along the 50 Ω transmission line can be detected by measuring the time evolution of the reflected voltage. A real impedance above 50 Ω yields a reflected step function with negative amplitude. If the transmission line is terminated by a capacitance, the time evolution of the voltage drop during charging of the capacitance equals the time dependence of the reflected voltage. Note that even after 15 ns, the voltage pulse is not fully absorbed by the sample, i.e., about 10% of its amplitude is still being reflected. As long as the pulse is applied, the absolute amplitude of the reflected voltage will rise towards saturation, which is reached at full charging up of the capacitance (further information is provided in the Supplemental Material [35]).

To further link the HF dynamics of the Schottky barrier to the pulsed electrical spin injection process, we depict a simple equivalent network of the sample in Fig. 3(c). In the reverse-bias regime, the Schottky contact can be modeled by a Schottky capacitance C_s and a parallel tunnel resistance R_s. The underlying n-GaAs detection layer is represented by a resistance R in series. We assume the displacement current I_c to be unpolarized, while the tunneling current I_t carries the spin-polarized electrons. The spin current $I_p = \eta I_t$ is given by the spin injection efficiency η. The charging and discharging of the Schottky capacitance is thus directly mapped to the temporal evolution of the spin current. I_p increases after the voltage pulse is turned on, whereas it decreases after the pulse is turned off after time Δw, i.e., during the discharge of C_s. If C_s, R_s, and η are approximately bias independent, the increase and decrease of I_p is single exponential,

$$I_p(t) = I_{p,dc} \times \begin{cases} 1 - d\exp\left(-\frac{t}{\tau_{sch}}\right) & 0 \leqslant t < \Delta w \\ \left[\exp\left(\frac{\Delta w}{\tau_{sch}}\right) - d\right]\exp\left(-\frac{t}{\tau_{sch}}\right) & \Delta w \leqslant t < T_{rep}, \end{cases} \tag{2}$$

and determined by the effective charge and discharge time τ_{sch} of the Schottky barrier, as illustrated in Fig. 3(d) for a pulse width of $\Delta w = 2$ ns and $\tau_{sch} = 6$ ns. The constant $d = [\exp(\frac{\Delta w - T_{rep}}{\tau_{sch}}) - 1]/[\exp(-\frac{T_{rep}}{\tau_{sch}}) - 1]$ is given by the boundary condition $I_p(0) = I_p(T_{rep})$.

It is important to emphasize that the temporal width of the electrically injected spin packet is determined by τ_{sch}. This temporal broadening becomes particularly important when individual spins start to precess in the external magnetic field at all times during the spin pulse. The retardation of spin precession results in spin dephasing of the spin packet. This phase "smearing" leads to a decrease of the net magnetization. Its temporal evolution can be estimated by

$$M_y(B_z, \Delta t) = \int_0^{\Delta t} dt\; r_S(t) M_0(\Delta t - t), \tag{3}$$

where $r_S(t) = I_p(t)/a$ is the spin injection rate with the active sample area a and where M_0 is given by an exponentially damped single-spin Larmor precession. The integral can be solved analytically (see Supplemental Material [35]) and results in a form as given qualitatively by Eq. (1) describing the dynamics of the injected spin packets, assuming $I_p(0) = 0$, i.e., $d = 1$. Note that the nonprecessing background signal of θ_F [see Fig. 2(a)] stems from the discharging of the Schottky capacitance, i.e., $\tau_{sch} = \tau_{bg}$, while T_2^* is not affected by the integration. This assignment is confirmed by the independent determination of τ_{sch} by TDR. The amplitude $A(B_z)$ in Eq. (1) becomes a function of ω_L, T_2^*, τ_{sch}, Δw, and r_s (see Eqs. (S17) and (S22) of the Supplemental Material [35]). For simulating $A(B_z)$, we take the above fitting results from Fig. 2, i.e., $T_2^*(B_z)$, ω_L, as well as $\Delta w = 2$ ns, and vary only τ_{sch} as a free parameter. The resulting field-dependent amplitudes are plotted in Fig. 2(d) at various time constants τ_{sch}. The experimental data are remarkably well reproduced for the τ_{sch} values determined by TDR ($\tau_{sch} = 6$ ns) and by the nonoscillatory background of θ_F ($\tau_{sch} = 8$ ns). This demonstrates that the charging and discharging of the Schottky capacitance is the main source of the amplitude drop in our experiment.

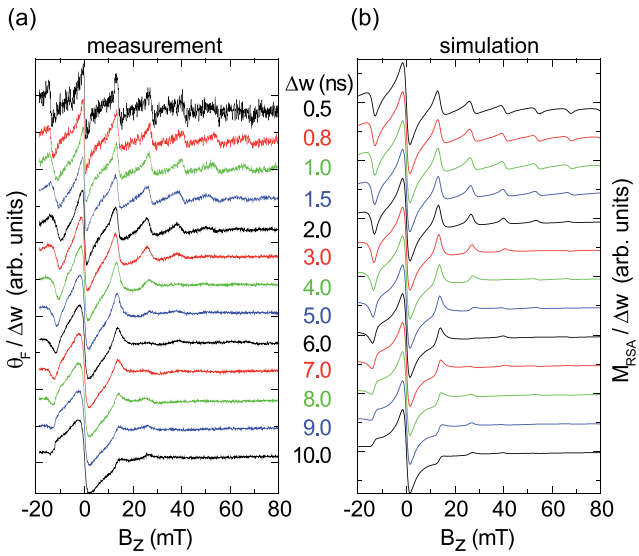

FIG. 4. Resonant spin amplification for various voltage pulse widths Δw. (a) Measured Faraday rotation θ_F normalized to Δw vs magnetic field B_z at $T_{\rm rep} = 12.5$ ns and fixed Δt with vertical offsets for clarity. (b) Simulations applying Eqs. (2) and (4) with $r_s(t)$ from Fig. 3(d) and $\tau_{\rm sch} = 6$ ns, $T_2^* = 18$ ns.

D. Resonant spin amplification

We now analyze the precession of the spin packets after injection with voltage pulses of different width Δw. This can be better tested as a function of the B field instead of in the time domain. To enhance the signal-to-noise ratio of θ_F, we reduce $T_{\rm rep}$ to 12.5 ns. As $T_{\rm rep}$ is now shorter than T_2^*, spin packets from subsequent voltage pulses can interfere. We thus enter the regime of resonant spin amplification (RSA) [3,4]. The net RSA magnetization $M_{y,RSA}$ results with Eq. (3) in

$$M_{y,RSA}(B_z, \Delta t) = M(\Delta t) + \sum_{n=1}^{\infty} \int_0^{T_{\rm rep}} dt\; r_S(t) M_0(\Delta t - t + nT_{\rm rep}), \quad (4)$$

where M_{RSA} and r_S are periodic in $T_{\rm rep}$ and defined in the time interval $[0, T_{\rm rep})$. Constructive interference of subsequent spin packets leads to a periodic series of resonances as a function of B, if a multiple of $1/T_{\rm rep}$ equals the Larmor frequency,

$$z/T_{\rm rep} = \omega_L/(2\pi), \quad (5)$$

where z is an integer.

Figure 4(a) shows RSA scans for Δw ranging between 500 ps and 10 ns taken at fixed Δt and normalized to Δw. Multiple resonances are observed for short $\Delta w \leqslant 2$ ns. The strong decrease of the resonance amplitudes with the increase of $|B_z|$ is consistent with the time-domain experiments (see Fig. 2). The number of resonances, which equals the number of Larmor precession cycles, subsequently decreases for broader current pulses. We observe a continuous crossover to the Hanle regime for the broadest pulses of $\Delta w = 10$ ns $\sim T_{\rm rep} = 12.5$ ns, which is close to the dc limit of spin injection, as shown in Fig. 1(b). This crossover strikingly demonstrates the phase triggering by the current pulses. While pulse-width induced phase smearing is observed above $\Delta w = 1.5$ ns, there are no effects of the pulse width below 1.5 ns due to the finite $\tau_{\rm sch}$. Remarkably, pulsed spin injection is possible for Δw as short as 500 ps.

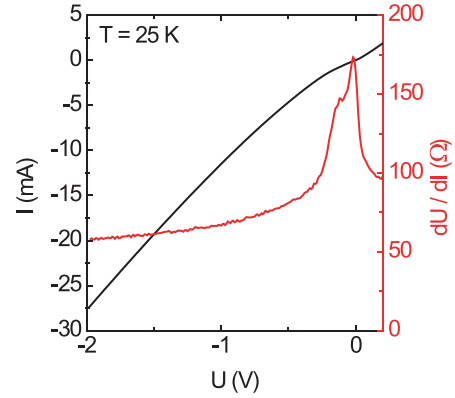

FIG. 5. IV-characteristics. The dc-current I as a function of dc-bias U (black line) and differential resistance dU/dI (red line) of the sample with 1300-μm-diameter mesa at 25 K. In our experiment, the Schottky diode is reverse biased using short -1.8 V voltage pulses.

The RSA scans are simulated using Eqs. (2) and (4) with $\tau_{\rm sch} = 6$ ns and are depicted in Fig. 4(b). The dependence on B_z as well as the phase "smearing" with increasing pulse width are well reproduced. Note that even the change of the RSA peak shape for higher-order resonances is reproduced by the simulations, demonstrating that our model explains all salient features of the experiment.

IV. CONCLUSION

In conclusion, we have shown that fast current pulses can trigger the macroscopic phase of spin packets electrically injected across an Fe/GaAs Schottky barrier. Current pulses having a width down to 500 ps trigger a spin imbalance observed as magnetic oscillations matching the effective electron

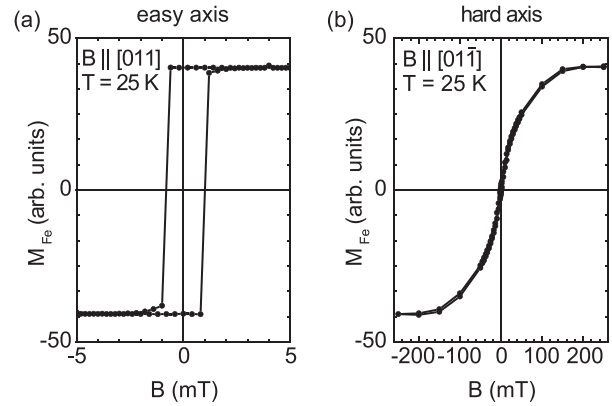

FIG. 6. Magnetic anisotropy of the Fe injector layer. In-plane magnetization of the epitaxial iron injector layer M_{Fe} as a function of the external magnetic field B as determined from superconducting quantum interference device (SQUID) measurements at 25 K. The B field is applied parallel to (a) the GaAs [011] and (b) the GaAs [01$\bar{1}$] crystal directions. The Fe injector layer exhibits an in-plane anisotropy. In our experiment, B is applied nearly parallel to the GaAs [01$\bar{1}$] direction (hard axis).

g factor of GaAs. Charging and discharging of the Schottky barrier yield a temporal broadening of the spin packets, resulting in a partial dephasing during spin precession. This partial spin dephasing manifests itself in a characteristic decrease of the oscillation amplitude as a function of the magnetic field and as a nonoscillating exponential decrease of the injected spin magnetization. Our model fully captures both of these features, which have not appeared when using ultrafast laser pulses for optical spin orientation, and it predicts that the time constant of the decreasing background is given by the discharging time constant of the Schottky barrier. This time constant independently determined by time-domain reflectometry well matches our observations of the phase smearing of the spin packet. Using a 10-times-higher frequency of the current pulses, we superimpose injected spin packets in GaAs and enter the regime of resonant spin amplification, which is well covered by our model as well. Our model predicts that the phase smearing can be significantly suppressed by reduction of the Schottky capacitance. In this respect, spin injection from diluted magnetic semiconductors will be advantageous for realizing all-electrical coherent spintronic devices of high-frequency bandwidth.

ACKNOWLEDGMENTS

This work was supported by HGF and by the Deutsche Forschungsgemeinschaft (DFG, German Research Foundation) under SPP 1285 (Grant No. 40956248). C.J.P. and P.A.C. acknowledge funding from the U.S. Office of Naval Research, the National Science Foundation (NSF) MRSEC program, the NSF NNIN program, and the University of Minnesota.

APPENDIX: SAMPLE CHARACTERISTICS

This section provides additional information about the sample used in our experiment. The I-V characteristics are displayed in Fig. 5. Magnetometry data of the Fe injector can be found in Fig. 6.

[1] R. Hanson and D. D. Awschalom, Nature (London) **453**, 1043 (2008).
[2] *Semiconductor Spintronics and Quantum Computing*, edited by D. D. Awschalom, D. Loss, and N. Samarth (Springer-Verlag, Berlin, 2002).
[3] J. M. Kikkawa and D. D. Awschalom, Phys. Rev. Lett. **80**, 4313 (1998).
[4] S. Kuhlen, R. Ledesch, R. de Winter, M. Althammer, S. T. B. Gönnenwein, M. Opel, R. Gross, T. A. Wassner, M. S. Brandt, and B. Beschoten, Phys. Status Solidi B **251**, 1861 (2014).
[5] L. Schreiber, D. Duda, B. Beschoten, G. Güntherodt, H.-P. Schönherr, and J. Herfort, Phys. Stat. Sol. B **244**, 2960 (2007).
[6] L. Schreiber, D. Duda, B. Beschoten, G. Güntherodt, H.-P. Schönherr, and J. Herfort, Phys. Rev. B **75**, 193304 (2007).
[7] K. Schmalbuch, S. Göbbels, Ph. Schäfers, Ch. Rodenbücher, P. Schlammes, Th. Schäpers, M. Lepsa, G. Güntherodt, and B. Beschoten, Phys. Rev. Lett. **105**, 246603 (2010).
[8] Y. K. Kato, R. C. Meyers, A. C. Gossard, and D. D. Awschalom, Nature (London) **427**, 50 (2003).
[9] S. A. Crooker and D. L. Smith, Phys. Rev. Lett. **94**, 236601 (2005).
[10] S. Kuhlen, K. Schmalbuch, M. Hagedorn, P. Schlammes, M. Patt, M. Lepsa, G. Güntherodt, and B. Beschoten, Phys. Rev. Lett. **109**, 146603 (2012).
[11] I. Stepanov, S. Kuhlen, M. Ersfeld, M. Lepsa, and B. Beschoten, Appl. Phys. Lett. **104**, 062406 (2014).
[12] S. A. Crooker, M. Furis, X. Lou, C. Adelmann, D. L. Smith, C. J. Palmstrøm, and P. A. Crowell, Science **309**, 2191 (2005).
[13] Y. K. Kato, R. C. Myers, A. C. Gossard, and D. D. Awschalom, Appl. Phys. Lett. **87**, 022503 (2005).
[14] X. Lou, C. Adelmann, S. A. Crooker, E. S. Garlid, J. Zhang, K. S. M. Reddy, S. D. Flexner, C. J. Palmstrøm, and P. A. Crowell, Nat. Phys. **3**, 197 (2007).
[15] I. Appelbaum, B. Huang, and D. J. Monsma, Nature (London) **447**, 295 (2007).
[16] B. Huang, D. J. Monsma, and I. Appelbaum, Phys. Rev. Lett. **99**, 177209 (2007).
[17] J. Li, B. Huang, and I. Appelbaum, Appl. Phys. Lett. **92**, 142507 (2008).
[18] Y. Ohno, D. K. Young, B. Beschoten, F. Matsukura, H. Ohno, and D. D. Awschalom, Nature (London) **402**, 790 (1999).
[19] R. Fiederling, M. Keim, G. Reuscher, W. Ossau, G. Schmidt, A. Waag, and L. W. Molenkamp, Nature (London) **402**, 787 (1999).
[20] H. J. Zhu, M. Ramsteiner, H. Kostial, M. Wassermeier, H.-P. Schönherr, and K. H. Ploog, Phys. Rev. Lett **87**, 016601 (2001).
[21] A. T. Hanbicki, B. T. Jonker, G. Itskos, G. Kioseoglou, and A. Petrou, Appl. Phys. Lett. **80**, 1240 (2002).
[22] A. T. Hanbicki, O. M. J. van't Erve, R. Magno, G. Kioseoglou, and C. H. Li, Appl. Phys. Lett. **82**, 4092 (2003).
[23] X. Jiang, R. Wang, R. M. Shelby, R. M. Macfarlane, S. R. Bank, J. S. Harris, and S. S. P. Parkin, Phys. Rev. Lett. **94**, 056601 (2005).
[24] C. Adelmann, X. Lou, J. Strand, C. J. Palmstrøm, and P. A. Crowell, Phys. Rev. B **71**, 121301(R) (2005).
[25] P. Kotissek, M. Bailleul, M. Sperl, A. Spitzer, D. Schuh, W. Wegscheider, C. H. Back, and G. Bayreuther, Nat. Phys. **3**, 872 (2007).
[26] V. G. Truong, P.-H. Binh, P. Renucci, M. Tran, Y. Lu, H. Jaffrès, J.-M. George, C. Deranlot, A. Lemaître, T. Amand *et al.*, Appl. Phys. Lett. **94**, 141109 (2009).
[27] P. Asshoff, W. Löffler, J. Zimmer, H. Füser, H. Flügge, H. Kalt, and M. Hetterich, Appl. Phys. Lett. **95**, 202105 (2009).
[28] C. H. Li, O. M. J. van 't Erve, and B. T. Jonker, Nat. Commun. **2**, 245 (2011).
[29] A. T. Hanbicki, S.-F. Cheng, R. Goswami, O. M. J. van 't Erve, and B. T. Jonker, Solid State Commun. **152**, 244 (2012).
[30] G. Schmidt, D. Ferrand, L. W. Molenkamp, A. T. Filip, and B. J. van Wees, Phys. Rev. B **62**, R4790(R) (2000).
[31] E. I. Rashba, Phys. Rev. B **62**, R16267 (2000).
[32] J. M. Kikkawa and D. D. Awschalom, Nature (London) **397**, 139 (1999).

[33] R. I. Dzhioev, K. V. Kavokin, V. L. Korenev, M. V. Lazarev, B. Y. Meltser, M. N. Stepanova, B. P. Zakharchenya, D. Gammon, and D. S. Katzer, Phys. Rev. B **66**, 245204 (2002).

[34] S. A. Crooker, M. Furis, X. Lou, P. A. Crowell, D. L. Smith, C. Adelmann, and C. J. Palmstrøm, J. Appl. Phys. **101**, 081716 (2007).

[35] See Supplemental Material at http://link.aps.org/supplemental/10.1103/PhysRevB.104.195202 for additional details on the modeling of the high-frequency dynamics of the pulsed spin injection process based on the equivalent network of the sample presented in Fig. 3(c).